Int J Adv Manuf Technol (2016) 84:1927–1939
DOI 10.1007/s00170-015-7782-y

ORIGINAL ARTICLE

On the application of 3D finite element modeling for small-diameter hole drilling of AISI 1045 steel

Xiaohui Nan[1] · **Lijing Xie**[1] · **Wenxiang Zhao**[1]

Received: 4 May 2015 / Accepted: 28 August 2015 / Published online: 23 September 2015

Abstract This paper studies the three-dimensional finite element (FE) modeling for simulating the small-hole drilling process of AISI 1045 by using FE package Abaqus/Explicit. The large deformation of work and the chip formation in drilling process is realized by incorporating Johnson-Cook material constitutive model and material failure criterion. In order to verify the simulation model, the simulation and corresponding drilling tests are performed for the drilling process with 3-mm diameter solid carbide drills at several combination groups of rotational speeds and feed velocities. The estimated thrust force, torque and chip morphology from the simulation are in good agreement with those tested from experiments. The combination of both simulations and experiments not only reveals obvious varying pattern of thrust force, torque with the increasing of rotational speeds and feed velocities, which is consistent with the cutting theory, but also provides a more detailed and profound knowledge about the cutting mechanism including the contribution of chisel edge, drilling stage, and stress and strain distribution, which is assumed to be helpful for the optimization of the drill structure, geometry and drilling parameters.

Keywords Finite element method · Small-hole drilling · 3D numerical simulation · AISI 1045

✉ Lijing Xie
rita_xie2004@163.com

[1] Beijing Institute of Technology, Beijing, China

1 Introduction

Drilling process is one of the most required machining techniques that accounts for more than 40 % of the total material removal processes and especially has a high frequency of use in aerospace industries [1]. It is significant to investigate the drilling mechanism. Though experimental method is a direct approach, it is time-consuming and inefficient to some extent. Numerical modeling method is widely considered as a valuable tool for predicting cutting forces, chip formation, tool wear, and distribution of important field variables such as strain, strain rate, temperatures, and stresses [2–4]. Plenty of research works on the development of 2D FE models were reported, ranging from material constitutive model and material failure criteria to tool-chip contact model, from turning and milling processes to grinding and drilling ones [5], from macro- to micro-machining, from homogeneous continuum [6] to multiphase materials [7], from chip formation simulation [8] to the prediction of residual stress and tool wear. The rapid development of high-performance computers and optimization of FE algorithm enables the 3D FE simulation. And, in order to make the simulation agree with the practical cutting conditions, some 3D models have been developed for the simulation of turning [9], milling [10], and grinding process [11] with general-purpose and specialized FE package such as Deform-3D, LS-DYNA, and ANSYS. In the consideration of the complicated geometry of drills and the combined action of multicutting edges and chisel edge in the actual material deformation in the cutting area, drilling process is far from being a 2D problem, and only a 3D FE simulation can interpret the drilling process properly.

Finite element models (FEM) for drilling of glass fiber reinforced plastic (GFRP) composite materials are proposed to

investigate the relative significance of speed, feed, and the point angle on the thrust force and torque [12, 13]. Durão et al. [14] also performed an FE analysis to calculate the thrust forces responsible for the defect at the exit of the hole drilling process of long-fiber composite structures. The thrust force and torque produced in drilling a composite laminate [15] and AISI 1040 work material with 10 mm-diameter drills [16] were investigated using 3D finite element models. Guo et al. established an FE simulation model for the drilling burr formation processes of 304-L stainless steel [17]. Muhammad et al. [18] developed a 3D FE model of drilling process using DEFORM-3D. They investigated the effect of an external heat source on the thrust force and torque of the drill-bit with an FE model and demonstrated the advantages of hot drilling of Ti alloys in reducing thrust force and torque. Wu et al. [19] used a simplified and idealized 3D FE model to analyze drilling process and predict drilling forces of titanium alloy Ti6Al4V. The study of Isbilir et al. [20] demonstrated the influence of drilling parameters on forces, burr, and work stress of titanium alloy with a 3D model.

The abovementioned studies mainly focus on the drilling process of normal-sized holes. However, with market's increasing calling for high-precision small-hole drilling technology, the simulation study on small-hole drilling is becoming necessary [21, 22], which is very helpful for the understanding of mechanism, development of innovative-structured drill, and optimization of drilling parameters. In small-hole drilling, the drill can be more easily fractured under the cutting force with the decrease of drill diameter and incurred weak stiffness. And, chip flow becomes more difficult, and sometimes chip accommodating space is choked by chips. Additionally, chatter becomes a very serious problem of small-hole drilling which deteriorates the hole quality and shortens the tool life greatly. The cooling of drill bit is rather difficult in the small-hole drilling. Especially, small-hole drilling of DTC materials such as high-strengthen steel and high-volume fraction PRMMC (Particle Reinforced Metal Matrix Composite) becomes more difficult to realize. According to drilling experiments of Zitoune et al. on composite material and aluminum stack, the greater drill diameter than 6 mm facilitates chip breaking [23]. Tsao et al. [24] evaluated delamination factor in drilling composite material using different drill diameters of 6, 8, and 10 mm. It was found that smaller diameter hole drilling was more likely to lead to delamination.

Otherwise, in former FE models, chip formation simulation of drilling process with perfect chip morphology is rarely realized with general-purpose FE packages. It is desired to build up a simulation including complicated geometry of the drill to establish material deformation and the chip formation. This study investigates not only thrust force and torque but also stress and strain distribution, chip morphology, and effect of chisel edge by both simulations and experiments.

As the beginning of a series study on small-hole drilling technology for typical difficult-to-cut (DTC) materials, this paper will aim to develop an effective simulation model for small-hole drilling process, taking AISI 1045 as the work material at present due to the accessibility of the material data.

2 3D finite element model of drilling process

In this study a 3D FE model for the drilling process has been developed using the FE package Abaqus/Explicit. The model is based on Lagrangian formulation. The complicated geometrical model of drill in numerical simulation is designed according to the parameters of actual drills used in experiments. The interaction between the drill and work which reflects the dynamic characteristics of drilling process is integrated by explicit dynamic analysis. Chip formation is one of the most significant results in this process so that element deletion has been implemented for the realization of chip's removal from the work.

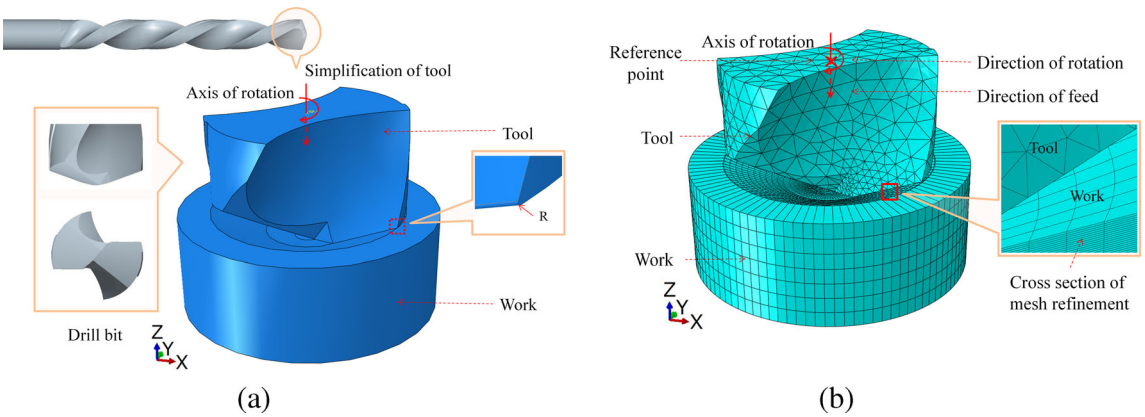

Fig. 1 The finite element model. **a** Geometry. **b** Initial mesh

Table 1 Mechanical and thermal properties of AISI 1045

Properties	Values							
Density, ρ(kg/m^3)	7800							
Poisson's ratio, v	0.3							
Young's modulus [26], E (GPa)	215		210		165		160	
at temperature T (°C)	20		200		400		600	
Thermal expansion [26, 27], α(×10^{-6}°C^{-1})	11	11	12	13	14	14	15	15
At temperature T (°C)	20	100	200	300	400	500	600	700
Specific heat capacity [28], C_p (J/kg/°C)	420+0.504 T							
Thermal conductivity [28], K (W/m/°C)	48.3–0.023 T							

2.1 Geometry modeling and meshing

In order to reduce the calculation time, only the drill bit and the neighboring part of the drill body are introduced into the drill model, as shown in Fig. 1. Very fine local mesh is used near the lips and chisel edge for the expression of the exact geometry of the edges and faces, due to their important role in the chip formation process. And, some detailed geometry characteristics, such as lip radius, are retained.

A small part of cylindrical work is modeled. A conical concave surface is pre-built on the work surface. In the drilling process, the drill is moved downward along the axis of the conical concave surface at the feed velocity. The mesh in the feed direction must be very fine in order to enable the simulation of chip formation. All the movements including the feed and rotation are exerted on a reference point on the drill's axis. The reference point imparts the movements to the drill. While all the freedoms of movement are constrained for the work.

2.2 Material properties and constitutive model

The JC constitutive material model [25] in Eq. (1) is applied to define material deformation since the metal cutting is a dynamic process accompanied by large strains, large strain rates, and thermal effects of material.

$$\sigma = (A + B\varepsilon^n)\left(1 + C\ln\frac{\dot{\varepsilon}}{\dot{\varepsilon}_0}\right)\left[1-\left(\frac{T-T_r}{T_m-T_r}\right)^m\right] \tag{1}$$

where σ is the equivalent flow stress, ε is the equivalent plastic strain, $\dot{\varepsilon}$ is the equivalent plastic strain rates, $\dot{\varepsilon}_0$ is the reference plastic strain rates, T is the work temperature, T_m is the melting temperature, and T_r is the room temperature, respectively. There are five parameters, i.e., A the yield strength of material, B hardening modulus, C strain rate sensitivity, n the strain hardening exponent, and m the thermal softening exponent. For medium steel AISI 1045, the mechanical and thermal properties are listed in Tables 1 and 2.

Chip separation in the simulation for drilling is much more difficult to realize than those in turning and milling. The existing chip separation criteria can be categorized into two groups, i.e., geometrical and physical. Geometrical ones are assumed to be inferior to the physical ones due to the lack of physical meanings. Thus, the physical ones are more suitable, and there are several options such as shear, Johnson and Cook damage law, strain energy density, effective strain, and strain energy density criteria in Abaqus/Explicit. Seeing that Johnson-Cook plasticity model is employed, Johnson-Cook damage law is introduced in this study.

When the equivalent plastic strain reaches the strain at failure ε_f^{pl}, thus, damage parameter ω exceeds 1, then damage occurs, and the element is removed from the mesh [30]. The damage parameter ω is defined as

$$\omega = \sum\left(\frac{\Delta\varepsilon^{pl}}{\varepsilon_f^{pl}}\right) \tag{2}$$

where $\Delta\varepsilon^{pl}$ is the increment in the equivalent plastic strain. The strain at failure is expressed as

$$\varepsilon_f^{pl} = \left[d_1 + d_2\exp\left(d_3\frac{p}{q}\right)\right] \times \left[1 + d_4\ln\left(\frac{\dot{\varepsilon}^{pl}}{\dot{\varepsilon}_0}\right)\right] \times \left[1 + d_5\left(\frac{T-T_r}{T_m-T_r}\right)\right] \tag{3}$$

where p is the hydrostatic pressure, q is the Von Mises stress, and other parameters were defined above. The

Table 2 Constants of Johnson-Cook model for AISI 1045 [29]

A (MPa)	B (MPa)	n	C	m	$\dot{\varepsilon}_0$ (s^{-1})	T_m(°C)	T_0(°C)
553.1	600.8	0.234	0.0134	1	0.001	1460	20

Table 3 Johnson-Cook failure parameters for AISI 1045 [31]

d_1	d_2	d_3	d_4	d_5
0.06	3.31	−1.96	0.0018	0.58

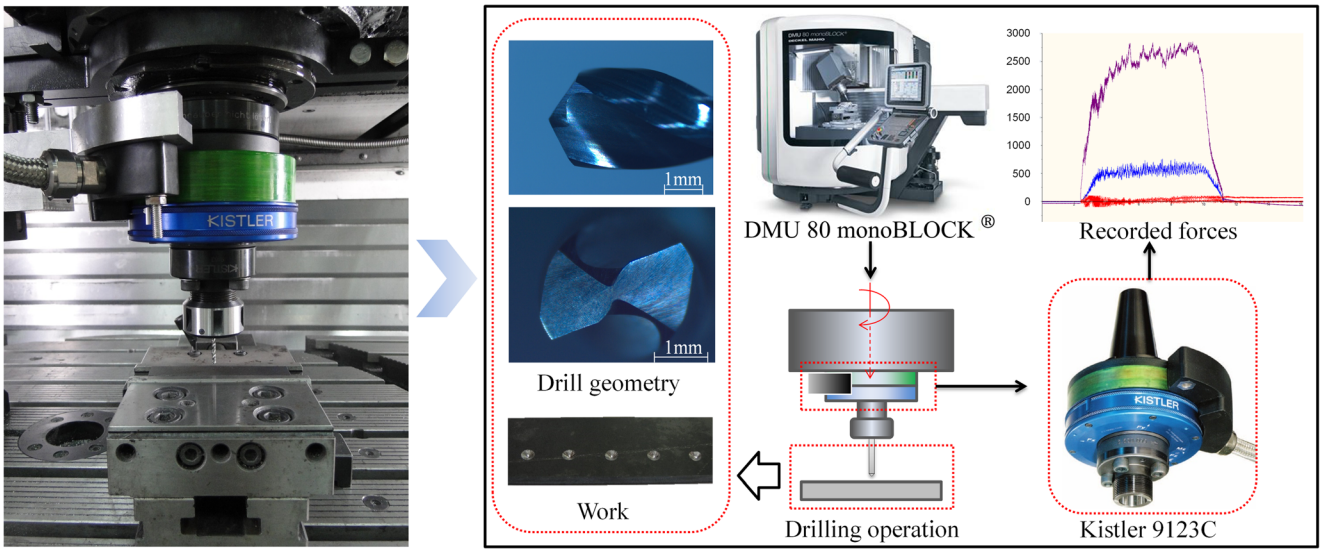

Fig. 2 Experiment setup

value of JC failure parameters $d_1 \sim d_5$ for AISI 1045 are listed in Table 3.

In addition, the cutting edges of drills move along a continuous, helix cutting path. It is fairly difficult to define a separation layer along the cutting path by setting helix partition surfaces on the work for narrowing down the implementation zone of Johnson-Cook damage law to decrease the calculation amount. Therefore, the Johnson-Cook damage law has to be defined for the entire drilling area of the work.

2.3 Tool-chip contact model

Özel [32] suggested that the friction modeling at the tool-chip interface has significant influence on the FE simulations of machining. Zorev [33] has divided tool-chip contact zone into sticking zone and sliding zones. Childs et al. [34] showed more complicated contact law incorporating the effect of cutting conditions, pressure, and temperature on the sticking and sliding zones at tool-chip interface. And, in most chip formation simulation works, the normal and shear flow stress on the tool rake face is described by Eq. (4).

$$\tau_f = \begin{cases} \mu\sigma_n & \mu\sigma_n < \tau_{\max} \quad \textit{sliding zone} \\ \tau_{\max} & \mu\sigma_n \geq \tau_{\max} \quad \textit{sticking zone} \end{cases} \tag{4}$$

The shear stress limit $\tau_{\max}$ is estimated as $\sigma_y/\sqrt{3}$, where σ_y is the yield stress of the work material adjacent to the tool-chip interface [35]. The division of contact zones and the friction parameters at the tool-chip interface is influenced by factors including cutting speed, feed rate, and rake angle [36]. A friction coefficient of 0.5 for machining AISI 1045 with carbide tools was used by Grzesik [37] at the cutting speed of 103.2 m/min. So, a friction coefficient of 0.6 is defined for this study in the consideration of the lower cutting speed.

3 Experimental verification

In order to verify the simulation model, nine drilling experiments of the complete combination of three rotational speeds and three feeds velocities are carried out on a CNC machining center DMU 80 monoBLOCK®. Thrust force and torque are measured by a rotating 4-Component Dynamometer RCD Kistler 9123, as shown in Fig. 2. The rotor of the dynamometer is installed on the spindle

Table 4 Drilling conditions and geometrical parameters

Rotational speed	1000, 2000, 3000 rpm
Feed velocity	50, 100, 150 mm/min
Cutting environment	Dry drilling
Tool material	K20 solid carbide
Tool diameter	3 mm
Point angle	140°
Helix angle	30°
Total length	56 mm
Work material	AISI 1045
Work size	100 mm×20 mm×3 mm

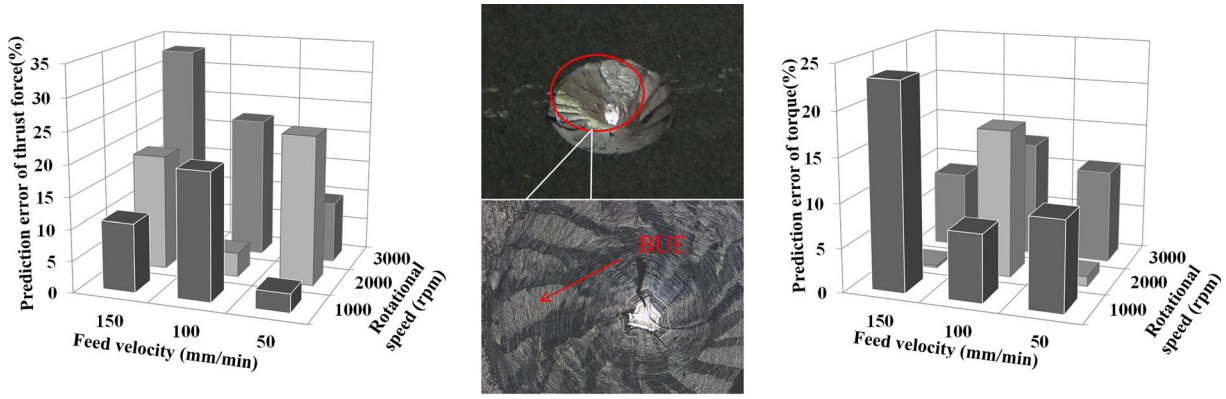

Fig. 3 Prediction error of thrust force and torque. **a** Thrust force. **b** BUE residue squeezed on the transition surface. **c** Torque

with the stator fixed nearby in a space of 1~3 mm, then the signal of drilling thrust force and torque can be collected. The twist drills employed in the experiments have the same geometry as that in simulations. The detailed parameters of experiments and drills are described in Table 4. The work used in experiment has a thickness of 3 mm. So, the work will be drilled through in a short time, e.g., 60 turns for the speed of 2000 rpm and 100 mm/min. A conical concave surface, which has the same conical shape of the drill tip, is prefabricated on the work surface. This is consistent with the simulation. The axis of the drill is aligned to that of the conical concave surface in machining. So, at the first contact of the work and the drill, both chisel edge and lips are engaged in the drilling work.

3.1 Thrust force and torque

In Fig. 3, the simulated thrust forces showed a 3.1–33.1 % error compared with measured forces and a better agreement of torques with a prediction in the range of 0.2–23.3 %. Due to the small hole-diameter limits, the drilling speed and the maximum cutting speed at the outermost edge is only 28.3 m/min, and the drilling process is companied by the frequent formation and vanishing of built-up edge (BUE), which results in the fluctuation of force and torque signals in experiments. On the other hand, the high-frequency fluctuation of simulation force and torque signals is observed too, and it is considered to be the product of coarse mesh of the work. Therefore, a larger prediction error is formed in small-hole drilling.

3.2 Chip morphology

Figure 4 shows the actual chip obtained in experiment and that from simulation in which the mesh size is refined and the simulation time is lengthened.

The final form of chip curling results from the combination of up-curling and side flow of chip. Even the chip's up curling in orthogonal cutting process is not a simple problem. Shaw assumed that chip's up curling is caused by the slightly curved shear plane due to the existence of

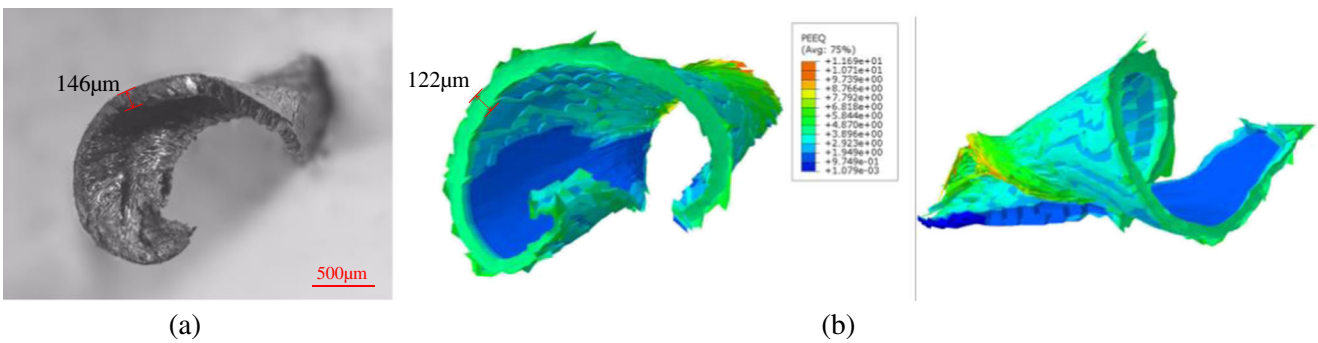

Fig. 4 Chip morphology at a rotational speed of 2000 rpm, feed velocity of 100 mm/min. **a** In experiment. **b** In simulation

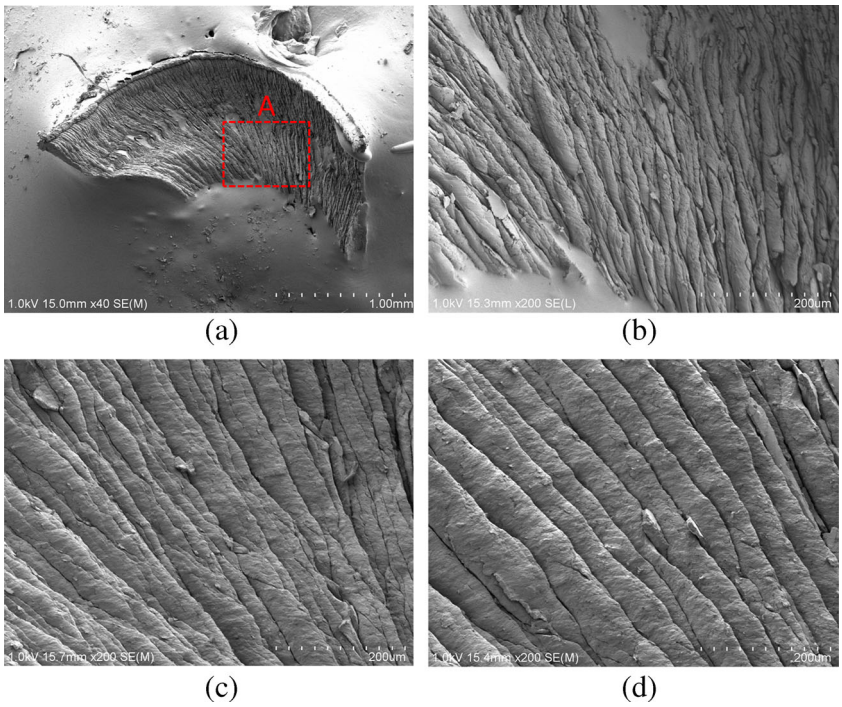

Fig. 5 SEM images of chip free surface morphology at **a**, **b** 50 mm/min, 1000 rpm, **c** 100 mm/min, 1000 rpm, and **d** 150 mm/min, 1000 rpm

BUE or equivalent secondary shear zone [38], while Astakhov proposed that nonuniform stress distribution on chip free surface and chip back surface caused by the bending moment [39] is the main reason. The chip curling in drilling process becomes extremely complex when the combined actions and the great variations of rake angle of chisel edge, lips, and margins of the drill and the side flow of chip are incorporated. Anyway, the simulated continuous chip type and the chip curling highly correspond to the actual chip appearance, and the predicted chip thickness error is within 16.4 %.

The equivalent plastic strain on the chip back surface is larger than that on the chip free surface due to the further plastic deformation by the serious friction at the tool-chip interface.

It is illustrated that lamella structure is most frequently observed on chips formed from most metallic materials [40, 41]. Figure 5 shows the image of chip free surface obtained

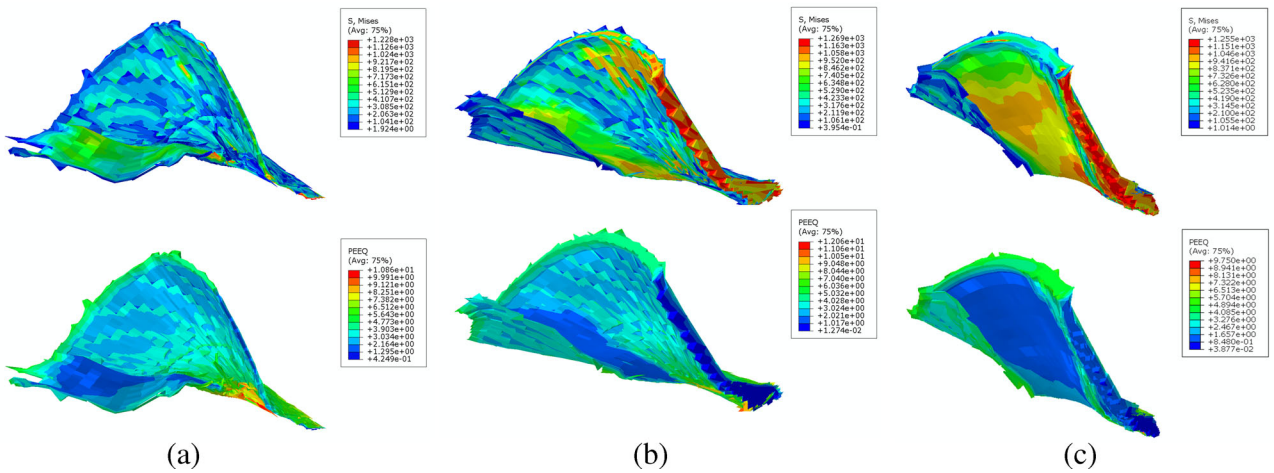

Fig. 6 Chips in simulations at **a** 50 mm/min, 1000 rpm, **b** 100 mm/min, 1000 rpm, and **c** 150 mm/min, 1000 rpm

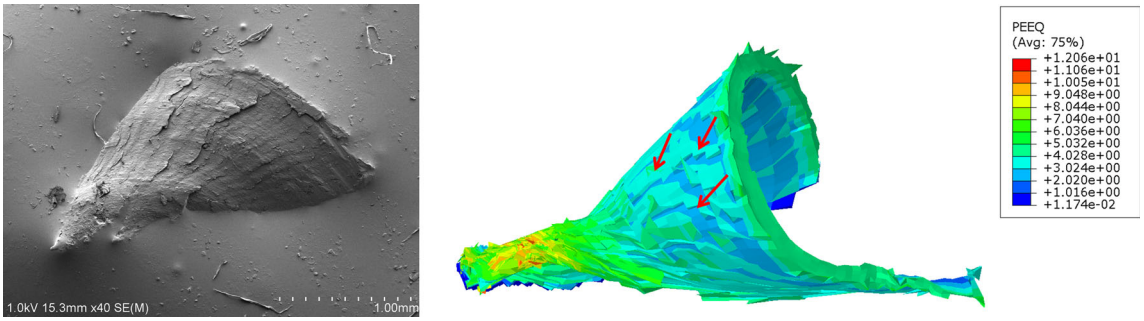

Fig. 7 Back surface of the chip in experiment and simulation at rotational speed of 1000 rpm, feed velocity of 100 mm/min

from the Hitachi S-4800 scanning electron micrograph (SEM). Figure 5b is the amplification of section A in Fig. 5a. The lamella structure on the chip free surface forms due to the crack initiation in the upper region of the primary shear zone. As the shear strain increases, a failure may occur because of the large strain of plastic deformation [42]. Moreover, experiments show that the interval of lamella is proportional to the feed per round. This expression of lamella in the simulation takes extremely fine mesh as a prerequisite, so no lamella structures are found on the simulated chip free surfaces in Fig. 6. Nonuniform distributed equivalent plastics strain and stress emerge on the chip free surfaces, and the extreme value distribution lines appear periodically and resemble the shape of drill's lip.

Figure 7 shows the back surface of the chip on which the wavy surfaces generated at rotational speed of 1000 rpm and feed velocity of 100 mm/min. This phenomenon is due to the uneven flow of chip on the blunt or rounded edge [43]. This type of surfaces can be also formed in simulations which are indicated by arrows.

4 Results and discussion

Small-hole drilling is characterized by the high-frequency drill breakage, short drill service life, drilling vibration, poor surface quality of drilled hole, etc., especially for DTC material such as high-strength steels. Although in this study, the small-hole drilling of AISI 1045 steel is taken as the study object, the modeling and analysis methods are applicable to DTC materials as well. Hence, the following analysis contents are organized in the goal of uncovering the specialties of small-hole drilling process, obtaining a complete understanding on the mechanism and further realizing the optimization of the drilling process parameters.

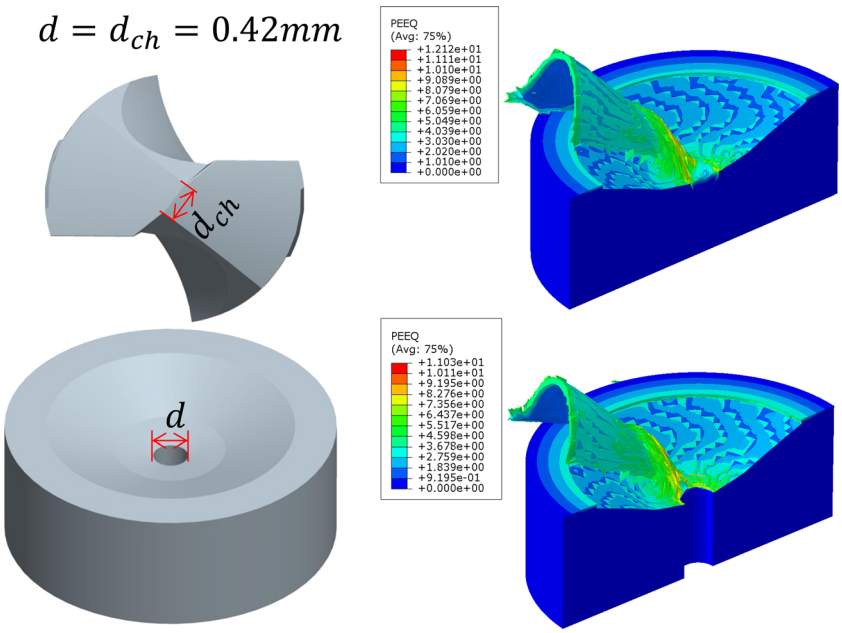

Fig. 8 Simulation of drilling with and without chisel action at rotational speed of 2000 rpm and feed velocity of 100 mm/min

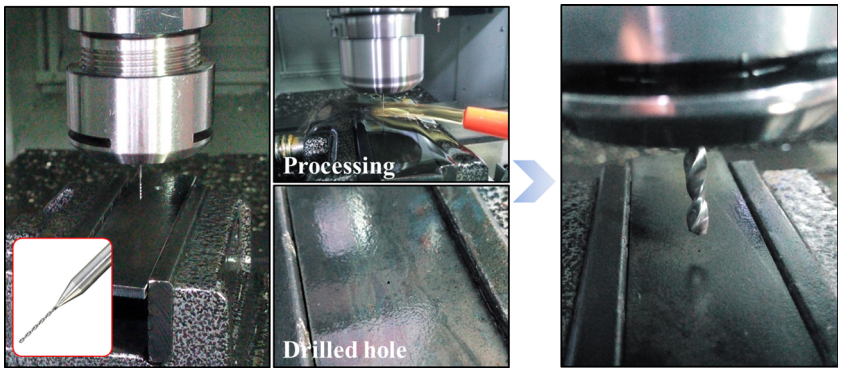

Fig. 9 Experiment setup and processing without chisel action

4.1 Contribution of chisel edge

In order to make clear the contribution of chisel edge, a simulation of drilling process along a pilot hole is performed, in which the pilot hole diameter is equal to the length of chisel edge, as shown in Fig. 8. The material under the chisel edge experiences strong squeezing action and flows away to form the central part of the spiral chips, and largest equivalent plastic strain appears here with a value nearly up to 10. And, the chip part next to the central part is formed by the cutting action of lip part with large negative rake angle, and the compound action of squeezing, ploughing, and cutting makes next largest equivalent plastic strain.

Experiments are carried out correspondingly to investigate the chisel action in drilling, as shown in Fig. 9. Pilot through-holes are drilled with customized 0.42-mm diameter drills firstly with sufficient cutting fluid supply, and then dry drilling is performed with 3-mm diameter drills along the axis of the pilot holes. The experiment is repeated for five times.

Figure 10a illustrates thrust force and torque with and without chisel action in the experiment. Since the chisel edge is not involved in cutting, the drilling force and torque are totally generated by the action of the lips and margins. The simulation shows that the chisel edge contributes to 25.6 % of thrust force and 2.5 % of torque respectively at the rotational speed of 2000 rpm and feed velocity of 100 mm/min. And, in the experiment, the chisel edge contributes 22.0 % of thrust force and 11.2 % of torque. But, according to the former study in [44], chisel edge has greater contributions, i.e., to thrust force higher than 50 % and to torque 25 %. This difference may be caused by the special structure of small-hole drill, on which larger web thickness is fabricated for strengthening the drill and the larger proportion of lips possessing negative rake angel will produce

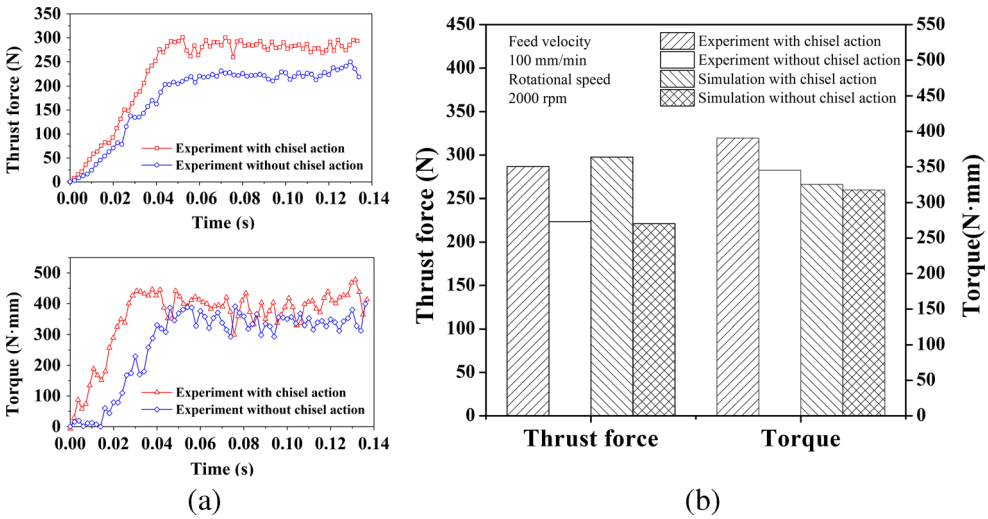

Fig. 10 Comparison of thrust force and torque with and without chisel action. **a** Variation of thrust force and torque vs. time in experiment. **b** Bar diagram of the comparison

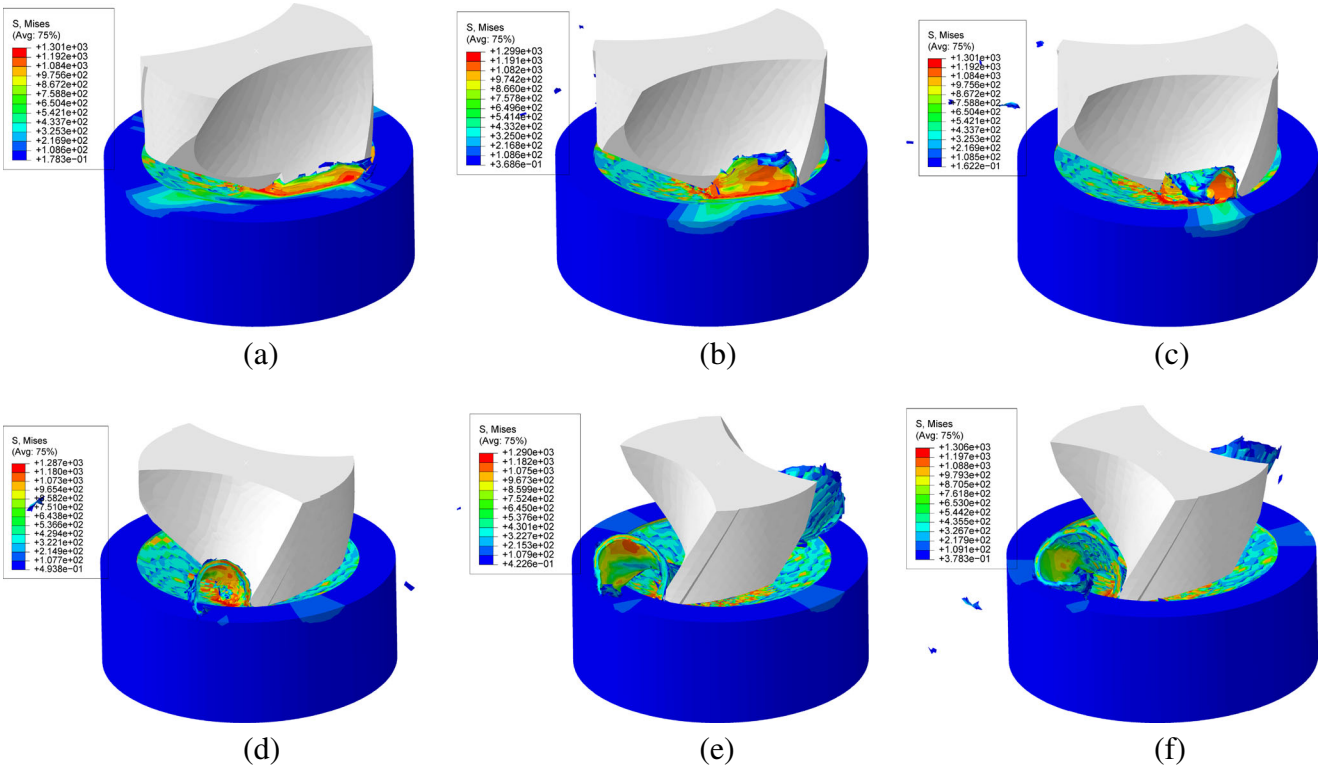

Fig. 11 Chip formation (tool diameter of 3 mm, rotational speed of 2000 rpm, feed velocity of 100 mm/min). **a** 0.010, **b** 0.015, **c** 0.018, **d** 0.022, **e** 0.026, and **f** 0.030 s

higher thrust force and torque, so the contribution of chisel edge is lowered. This reasoning needs to be tested in the future's study. If so, the idea to avoiding the premature breakage of drill in small-diameter drilling of DTC materials by prefabricating a tiny pilot hole with laser or EDM drilling method and then drilling to the final diameter along the pilot hole may not be effective, and developing a new structure drill will become necessary.

4.2 Chip formation and stress distribution

Figure 11 shows clearly the formation and growth of the chips with the advance of drill bit into the work. Two pieces of continuous chips are forming under the combined action of the lips and the chisel edges and flowing out along the flutes. In the drilling process, the high stress is always located at primary shear zone and chisel edge's squeezing zone, and follows the moving of these two zones. Especially the maximum von Mises stress appears at the intersection of lips and margins, where the work material is undergoing higher equivalent strain and lower hydrostatic pressure than that at other places of the primary shear zone.

Figure 12 shows chip formation at various rotational speeds and feed velocities. The maximum von Mises stress maintains located at the outmost of the primary shear zone and increases with the feed velocity due to the increasing of cutting thickness and increases with the rotation speed when keeping the feed rate per round unchanged. In addition, the chip thickness increases with the feed velocity from 50 to 150 mm/min, as shown in Fig. 12a–c. When the rotational speed goes up from 1000 to 3000 rpm, i.e., from 9.42 to 28.27 m/min with a constant feed rate of 0.05 mm/rev, as shown in Fig. 12a, d, the chip becomes thinner and easier to break under the effect of higher stress, which confirms to the actual chips in Fig. 12e. In addition, at 3000 rpm, rather irregular chip may be produced by the uneven chip flow and the variation of cutting thickness due to the high-frequency growth and death of BUEs [42].

4.3 Drilling stage

Because of the existence of prefabricated conical concave surface on the work, the uncut thickness at the lips and chisel edge will simultaneously increase from 0 to a stable

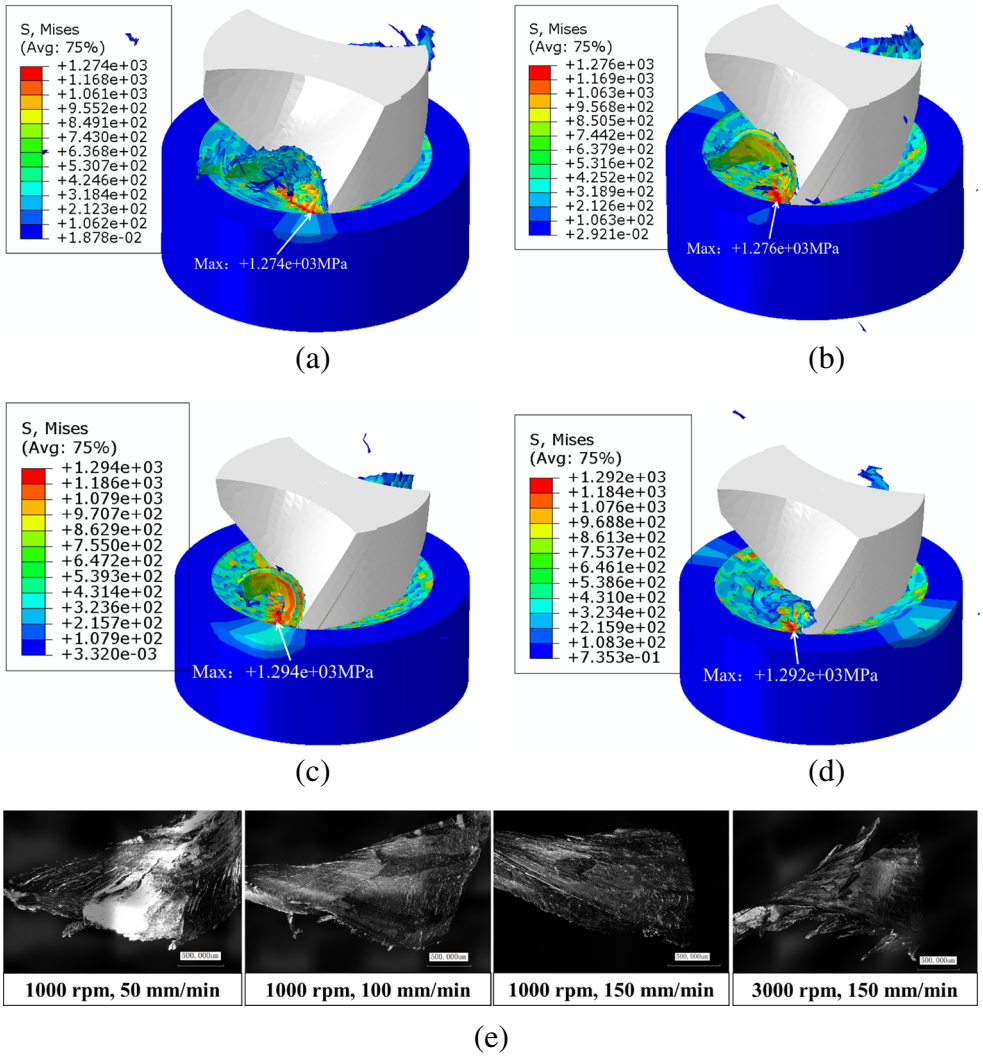

Fig. 12 Chip formations at different rotational speeds and feed velocities. **a** 1000 rpm, 50 mm/min; **b** 1000 rpm, 100 mm/min; **c** 1000 rpm, 150 mm/min; and **d** 3000 rpm, 150 mm/min. **e** Chip formed at different drilling parameters in experiment

value in the first turn of drilling. This happens in the first turn of 0.03 s under the cutting condition of Fig. 13. So, the torque firstly experiences an increasing stage with some small fluctuations within the first 0.03 s and then keeps stable hereafter. But, the increasing stage of thrust force takes a longer time, about 0.05 s. This difference can be explained by the contribution of lips and chisel edge to torque and thrust force and their rake angel's variation. Most of the torque is due to the cutting action of the lips, because the drill radius along the lips is longer than the radius along the chisel edge. The torque will go up with the increasing of the uncut thickness in the first turn. In the later turns, the uncut thickness has no change, so the torque will fluctuate in the vicinity of a certain value. As for the thrust force, it is considered to be mainly caused by the cutting action at the chisel edge [4, 7] because the chisel edge is characterized by large negative rake angle. Only when the uncut thickness reaches a relatively high value, the chip formation can take place. Therefore, at the beginning, thrust force is only caused by ploughing and extruding the work material toward the lips without cutting.

Larger fluctuation of the thrust force and torque curves than that of experimental data in Fig. 13 is observed. And, the fluctuation in simulation is expected to be reduced by further refining the work mesh, whereas the stage division and average value of drilling thrust force and torque in the simulation and experiment have a good agreement.

4.4 The effect of cutting parameters on force and torque

Figure 14 shows the influence of rotational speed and feed velocity on thrust force and torque evidently. Both the thrust

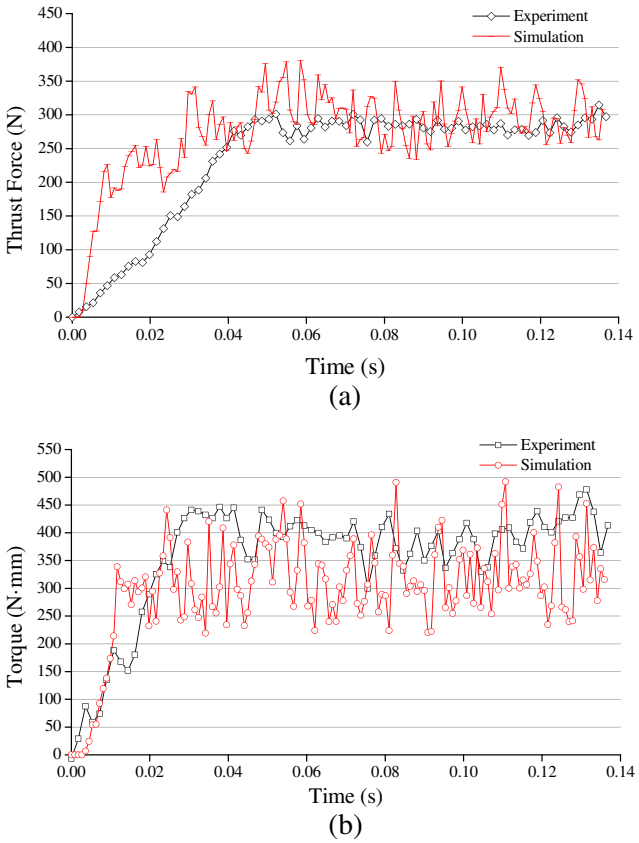

Fig. 13 Thrust force and torque obtained from experiment and simulation (tool diameter of 3 mm, rotational speed of 2000 rpm, feed velocity of 100 mm/min). **a** Thrust force. **b** Torque

forces and torque decrease significantly with the increase of rotational speed at the three feed velocities. In addition, it can be observed that increasing feed velocity results in the increase of thrust force and torque. In drilling process, either increase in feed velocity or decrease in rotational speed increases the uncut chip thickness and the cutting area, finally causing thrust force and torque increased. But, if the feed remains constant in drilling, e.g., 0.05 mm/rev, rotational speed in the examined range from 1000 to 3000 rpm has little influence on both thrust force and torque. Hence, a combination of lower feed velocity and higher rotation speed is preferred for improving drilling stability and preventing drill failure.

5 Conclusions

Small-hole drilling process of AISI 1045 steel is investigated by a developed 3D FE model including contribution of chisel edge, chip formation, stress distribution, drilling stage, thrust force, and torque. And, the following conclusions have been drawn.

1. The 3D FE model of small-hole drilling is verified by thrust force, torque, and chip morphology tested from the experiment. The prediction error of thrust force is less than 33.1 % and the torque 23.3 %, and refining the work's mesh is assumed to be able to lower the prediction error.
2. Small diameter drill is strengthened by large web thickness, so large portion of lips possess negative rake angle. This lowers the chisel edge's contribution to thrust force and torque in small-hole drilling. Development of new structure drill and optimization of drilling parameters in performing small-hole drilling on DTC materials may be more effective than drilling to the final diameter along a prefabricated pilot hole.
3. High stress always appears at the primary shear zone; moreover, maximum von Mises stress value is located at the intersection of lips and margins regardless of the drilling parameters, whereas maximum equivalent plastic strain appears at the squeezing zone of chisel edge and high equivalent plastic strain are formed at the intersection of lips and margins because of the larger deformation.

Acknowledgments This work is supported by the National Key Projects of Science and Technology of China (Item No.:2012ZX04003051-3).

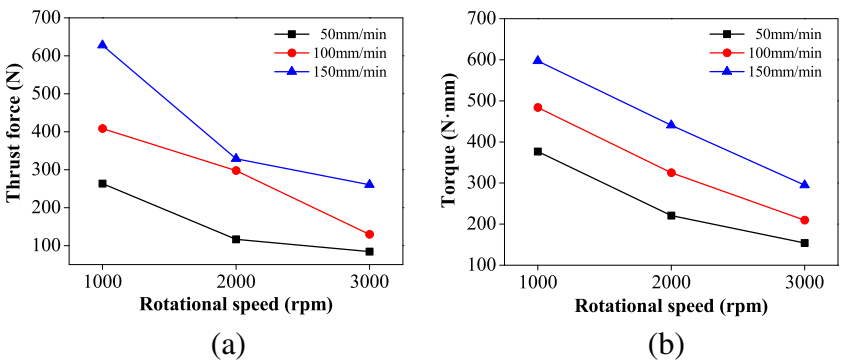

Fig. 14 Variation of simulated data with different rotational speeds and feed velocities. **a** Thrust force. **b** Torque

References

1. Gaitonde VN, Karnik SR, Siddeswarappa B, Achyutha BT (2008) Integrating Box-Behnken design with genetic algorithm to determine the optimal parametric combination for minimizing burr size in drilling of AISI 316L stainless steel. Int J Adv Manuf Technol 37(3–4):230–240. doi:10.1007/s00170-007-0957-4
2. Ozel T, Altan T (2000) Determination of workpiece flow stress and friction at the chip–tool contact for high-speed cutting. Int J Mach Tool Manuf 40(1):133–152. doi:10.1016/S0890- 6955(99)00051-6
3. Tang L, Huang J, Xie L (2011) Finite element modeling and simulation in dry hard orthogonal cutting AISI D2 tool steel with CBN cutting tool. Int J Adv Manuf Technol 53:1167–1181. doi:10.1007/s00170-010-2901-2
4. Deng WJ, Xia W, Tang Y (2009) Finite element simulation for burr formation near the exit of orthogonal cutting. Int J Adv Manuf Technol 43:1035–1045. doi:10.1007/s00170-008-1784-y
5. Guu YH, Deng CS, Hou MT, Hsu CH, Tseng KS (2012) Optimization of machining parameters for stress concentration in microdrilling of titanium alloy. Mater Manuf Process 27(2):207–213. doi:10.1080/10426914.2011.566657
6. Davim JP, Maranhão C (2009) A study of plastic strain and plastic strain rate in machining of steel AISI 1045 using FEM analysis. Mater Des 30(1):160–165. doi:10.1016/j.mat-des.2008.04.029
7. Zhou L, Huang ST, Wang D, Yu XL (2011) Finite element and experimental studies of the cutting process of SiCp/Al composites with PCD tools. Int J Adv Manuf Technol 52:619–662. doi:10.1007/s00170-010-2776-2
8. Zhang YC, Mabrouki T, Nelias D, Gong YD (2011) Chip formation in orthogonal cutting considering interface limiting shear stress and damage evolution based on fracture energy approach. Finite Elem Anal Des 47(7):850–863. doi:10.1016/j.finel.2011.02.016
9. Özel T (2009) Computational modelling of 3D turning: influence of edge micro-geometry on forces, stresses, friction and tool wear in PcBN tooling. J Mater Process Technol 209(11):5167–5177. doi:10.1016/j.jmatprotec.2009.03.002
10. Maurel-Pantel A, Fontaine M, Thibaud S, Gelin JC (2012) 3D FEM simulations of shoulder milling operations on a 304L stainless steel. Simul Model Pract Theory 22:13–27. doi:10.1016/j.simpat.2011.10.009
11. Mao C, Zhou ZX, Ren YH, Zhang B (2010) Analysis and FEM simulation of temperature field in wet surface grinding. Mater Manuf Process 25(6):399–406. doi:10.1080/1042691-0903124811
12. Singh I, Bhatnagar N, Viswanath P (2008) Drilling of unidirectional glass fiber reinforced plastics: experimental and finite element study. Mater Des 29(2):546–553. doi:10.1016/j.matdes.2007.01.029
13. Isbilir O, Ghassemieh E (2012) Finite element analysis of drilling of carbon fibre reinforced composites. Appl Compos Mater 19(3–4):637–656. doi:10.1007/s10443-011-9224-9
14. Durão LMP, De Moura M, Marques AT (2008) Numerical prediction of delamination onset in carbon/epoxy composites drilling. Eng Fract Mech 75(9):2767–2778. doi:10.1016/j.engfrac-mech.2007.03.009
15. Phadnis VA, Makhdum F, Roy A, Silberschmidt VV (2013) Drilling in carbon/epoxy composites: experimental investigations and finite element implementation. Compos A:Appl Sci 47:41–51. doi:10.1016/j.compositesa.2012.11.020
16. Gök K, Türkes E, Neseli S, Saglam H, Gök A (2013) The validation as experimental and numerical of the values of thrust force and torque in drilling process. J Eng Sci Technol Rev 6(3):93–99
17. Guo YB, Dornfeld DA (2000) Finite element modeling of burr formation process in drilling 304 stainless steel. J Manuf Sci Eng 122(4):612–619. doi:10.1115/1.1285885
18. Muhammad R, Ahmed N, Shariff YM, Silberschmidt VV (2012) Finite-element analysis of forces in drilling of Ti-alloys at elevated temperature. Solid State Phenom 188:250–255. doi:10.4028/www.scientific.net/SSP.188.250
19. Wu HB, Jia ZX, Zhang XC, Liu G (2012) Study on simulation and experiment of drilling for titanium alloys. Mater Sci Forum 704:657–663. doi:10.4028/www. scientific.net/MSF.704-705.657
20. Isbilir O, Ghassemieh E (2011) Finite element analysis of drilling of titanium alloy. In: 11th International Conference on the Mechanical Behavior of Materials 10: 1877–1882. doi: 10.1016/j.proeng.2011.04.312
21. Endo H, Murahashi T, Marui E (2007) Accuracy estimation of drilled holes with small diameter and influence of drill parameter on the machining accuracy when drilling in mild steel sheet. Int J Mach Tool Manuf 47(1):175–181. doi:10.1016/j.ijmachtools.2006.02.001
22. Liu HT (2007) Hole drilling with abrasive fluidjets. Int J Adv Manuf Technol 32(9–10):942–957. doi:10.1007/s00170-005-0398-x
23. Zitoune R, Krishnaraj V, Collombet F (2010) Study of drilling of composite material and aluminium stack. Compos Struct 92(5):1246–1255. doi:10.1016/j.compstruct.2009.10.010
24. Tsao CC, Hocheng H (2004) Taguchi analysis of delamination associated with various drill bits in drilling of composite material. Int J Mach Tool Manuf 44(10):1085–1090. doi:10.1016/j.ijmachtools.2004.02.019
25. Johnson GR, Cook WH (1983) A constitutive model and data for metals subjected to large strains, high strain rates and high temperatures. In: Proceedings of the seventh international symposium on ballistics, Hague, pp. 541–547
26. Iqbal SA, Mativenga PT, Sheikh MA (2007) Characterization of machining of AISI 1045 steel over a wide range of cutting speeds. Part 2: evaluation of flow stress models and interface friction distribution schemes. P I Mech Eng B J Eng 221(5):917–926. doi:10.1243/ 09544054JEM797
27. Rech J, Claudin C, D'Eramo E (2009) Identification of a friction model—application to the context of dry cutting of an AISI 1045 annealed steel with a TiN-coated carbide tool. Tribol Int 42(5):738–744. doi:10.1016/j.triboint.2008.10.007
28. Adibi-Sedeh AH, Vaziri M, Pednekar V, Madhavan V, Ivester RW (2005) Investigation of the effect of using different material models on finite element simulations of machining. In: Proceeding of the 8th CIRP International Workshop on Modeling of Machining Operations, Chemnitz, Germany, pp. 215–224
29. Jaspers S, Dautzenberg JH (2002) Material behaviour in conditions similar to metal cutting: flow stress in the primary shear zone. J Mater Process Tech 122(2):322–330. doi:10.1016/S0924-0136(01)01228-6
30. Abaqus 6.11 Documentation. Abaqus/CAE user's manual, 2011
31. Duan CZ, Dou T, Cai YJ, Li YY (2009) Finite element simulation and experiment of chip formation process during high speed machining of AISI 1045 hardened steel. Int J Recent Trends Eng 1(5):46–50
32. Özel T (2006) The influence of friction models on finite element simulations of machining. Int J Mach Tool Manuf 46(5):518–530. doi:10.1016/j.ijmachtools.2005.07.001
33. Zorev NN (1963) Inter-relationship between shear processes occurring along tool face and shear plane in metal cutting. Int Res Prod Eng 42–49
34. Childs THC, Maekawa K (1990) Computer-aided simulation and experimental studies of chip flow and tool wear in the turning of low alloy steels by cemented carbide tools. Wear 139:235–250
35. Liu CR, Guo YB (2000) Finite element analysis of the effect of sequential cuts and tool–chip friction on residual stresses in a machined layer. Int J Mech Sci 42:1069–1086. doi:10.1016/S0020-7403(99)00042-9

36. Haglund AJ, Kishawy HA, Rogers RJ (2008) An exploration of friction models for the chip–tool interface using an Arbitrary Lagrangian–Eulerian finite element model. Wear 265(3):452–460. doi:10.1016/j.wear.2007.11.025
37. Grzesik W (2006) Determination of temperature distribution in the cutting zone using hybrid analytical–FEM technique. Int J Mach Tool Manuf 46(6):651–658. doi:10.1016/j.ijmach- tools.2005.07.009
38. Shaw MC (2004) Metal cutting principals. Oxford University Press, USA
39. Astakhov VP (2006) Tribology of metal cutting, 1st Ed. Elsevier Science Publishing Company
40. Barry J, Byrne G (2002) The mechanisms of chip formation in machining hardened steels. J Manuf Sci Eng Trans ASME 124: 528–535. doi:10.1115/1.1455643
41. Sun J, Guo YB (2008) A new multi-view approach to characterize 3D chip morphology and properties in end milling titanium Ti-6Al-4 V. Int J Mach Tools Manuf 48:1486–1494. doi:10.1016/j.ijmachtools.2008.04.002
42. Farid AA, Sharif S, Idris MH (2011) Chip morphology study in high speed drilling of Al-Si alloy. Int J Adv Manuf Technol 57(5–8):555–564. doi:10.1007/s00170-011-3325-3
43. Trent EM, Wright PK (2000) Metal cutting, 4th edn. Butterworth–Heinemann, Massachusetts
44. Paul A, Kapoor SG, DeVor RE (2005) Chisel edge and cutting lip shape optimization for improved twist drill point design. Int J Mach Tool Manuf 45(4):421–431. doi:10.1016/ j.ijmachtools.2004.09.010